

# Measurement of jet fragmentation in $p + p$ collision at $\sqrt{s} = 200$ GeV with the PHENIX detector

Yue-shi Lai (for the PHENIX Collaboration)

Columbia University, New York, NY 10027-7061 and Nevis Laboratories, Irvington, NY 10533-2508, USA

E-mail: ylai@phys.columbia.edu

**Abstract.** Measurement of jet fragmentation property in  $p + p$  collisions provides a crucial baseline for the study of a possible, modified fragmentation behavior at the presence of the quark-gluon plasma. We describe the first measurement of jet fragmentation functions in  $\sqrt{s} = 200$  GeV  $p + p$  collisions at RHIC. This is facilitated by extending the linear least square unfolding technique employed by high energy and nuclear experiments to multidimensional spectra, which allows us to correct the inefficiencies in the jet energy response encountered at detectors such as PHENIX.

## 1. Introduction

Hadronization of jet production into final state particles, together with the production of hard scattering, are complementary parts of the QCD description of particle production. Fragmentation function in  $p + p$  collisions further provides a baseline for any measurement of the fragmentation property of reconstructed jets in heavy ion collisions. The narrow detector aperture and the need to operate within the large multiplicity heavy ion background has traditionally limited the application of direct jet reconstruction at PHENIX. Fragmentation properties of jet production therefore been only measured via two particle correlations by PHENIX [1, 2]. The Gaussian filter jet reconstruction algorithm [3] provides a cone-like algorithm that at the same time reduces the sensitivity to large angle fragments (or the lack of such, due to acceptance limit), and is therefore well-suited for both  $p + p$  and heavy ion measurement at PHENIX.

Measurement of fragmentation function using a detector with inefficiency due to the lack of hadronic calorimetry is difficult, since the full jet energy is not directly accessible, but has to be reconstructed from combining track momenta with the electromagnetic cluster energies. While the energy carried by long-lived neutral hadrons such as  $n$ ,  $K_L^0$  are fully lost, the inherent momentum resolution and background in a typical tracking system limits the ability to accurately measure tracks with  $p \gg 20$  GeV/ $c$ . The resulting large difference in the true and measured jet energy scale is difficult to correct multiplicatively, but can be addressed by using unfolding the measured spectra with the true-to-detector-level jet energy transfer function. This is particularly difficult for spectra that contain additional dimensions than the jet energy, such as the fragmentation function. As such, none of the RHIC experiment, which all lacks hadronic calorimetry, has attempted the measurement of fragmentation functions so far.

Jet reconstruction using the  $\sigma_{\text{filter}} = 0.3$  Gaussian filter has been applied to PHENIX for the measurement of the inclusive jet cross section in  $p + p$  and jet yield in Cu + Cu [4, 5]. In this proceeding, we report the development of a multidimensional unfolding technique for the energy scale correction of fragmentation functions, and the measurement of  $p + p$  fragmentation functions for charged particles and neutral electromagnetic clusters using the PHENIX detector.

## 2. Jet reconstruction by Gaussian filtering

The iterative cone algorithm with the size parameter  $R$  is known to be equivalent to a local maximization of a filter output in  $(\eta, \phi)$  with a special choice of the angular weight function to be the flat  $k(r^2) = \theta(R^2 - r^2)$  and  $r^2 = \eta^2 + \phi^2$  (note that unlike  $k(r^2)$ , the filter kernel is  $h(r^2) \propto -\int dr^2 k(r^2) \propto \max(0, 1 - r^2/R^2)$ , and not flat) [6, 7]. Similarly, the Gaussian filter uses a Gaussian distributed weighting. The Gaussian weighting takes advantage the property of high- $p_T$  jets being collimated emissions of particles, and enhances the center signal to the periphery, which is more likely to be contaminated by the event background. By avoiding an sharp radial cut-off, the algorithm also becomes analytically collinear and infrared safe (we further verified the practical infrared safety using a procedure analogously to [8]).

In  $p + p$  events and without a large event background, the event transverse momentum density is the sum of point-like final state particles  $p_{T,i}$

$$p_T(\eta, \phi) = \sum_{i \in F} p_{T,i} \delta(\eta - \eta_i) \delta(\phi - \phi_i). \quad (1)$$

The Gaussian filtering of  $p_T$  is the linear-circular convolution of  $p_T(\eta, \phi)$  with a Gaussian distribution

$$p_T^{\text{filt}}(\eta, \phi) = \iint d\eta' d\phi' p_T(\eta', \phi') \exp\left(-\frac{(\eta - \eta')^2 + (\phi - \phi')^2}{2\sigma_{\text{filter}}}\right). \quad (2)$$

The output of the filter for a given  $(\eta, \phi)$  position is the Gaussian weighted transverse momentum in the said event. The local maxima in  $p_T^{\text{filt}}(\eta, \phi)$  are the reconstructed jets using the Gaussian filter. More detailed discussion of the property of Gaussian filter for jet reconstruction can be found in [3, 5].

## 3. Multidimensional unfolding

The true particle level and the measured energy scale in the PHENIX central arm differ due to inefficiencies, the lack of hadronic calorimetry, and the loss of out-of-acceptance fragments due to the  $\Delta\eta = 0.7$  pseudorapidity coverage and also the  $\Delta\phi = \pi$  partial azimuthal coverage. This difference means that a full unfolding is needed to extract the true energy instead of a first order multiplicative correction.

Linear least square unfolding with the Phillips–Tikhonov regularization [9, 10] has been widely used by e.g. GURU [11] for the unfolding of spectra. Binned spectra can be mathematically regarded as a vector of individual bins, and the linear bin-to-bin migration due to differing energy scales is then conveniently expressed as a matrix. For a typical transfer matrix  $\mathbf{A}$  generated using Monte Carlo detector simulation, if the measured spectrum  $\mathbf{b}$  with the covariance matrix  $\mathbf{C}$  is unfolded using the simple linear least square relation

$$\underset{\mathbf{x}}{\text{minimize}} \quad \|\mathbf{Ax} - \mathbf{b}\|_{\mathbf{C}}^2, \quad (3)$$

( $\|\mathbf{u}\|_{\mathbf{C}} = \mathbf{u}^T \mathbf{C}^{-1} \mathbf{u}$  denotes the Mahalanobis distance) the propagation of fluctuations in  $\mathbf{A}$  would result in large, non-statistical fluctuation in the unfolding result  $\mathbf{x}$ . The regularized unfolding determines the unfolded spectrum  $\mathbf{x}$  by solving the minimization problem

$$\underset{\mathbf{x}}{\text{minimize}} \quad \|\mathbf{Ax} - \mathbf{b}\|_{\mathbf{C}}^2 + \tau \|\mathbf{Lx}\|^2, \quad (4)$$

where  $\tau$  is the regularization parameter and  $\mathbf{L}$  is a linear operator that describes the amount of discontinuity or “noisiness” of the unfolding result.

Spectra in particle and nuclear physics can cross multiple orders of magnitude and a homogeneous  $\mathbf{L}$  would cause the large magnitude part of the spectra to dominate the singular vectors, thus exhausting most degrees of freedom purely to reproduce the variation in magnitudes. This can be solved by either scaling  $\mathbf{L}$  to approximately match the variations in  $\mathbf{x}$ , or to prescale  $\mathbf{x}$ . We follow the approach used by GURU to prescale the unknowns by

$$x_i \mapsto \hat{x}_i = \frac{x_i}{x_i^{\text{ini}}}, \quad (5)$$

and the linear system  $\mathbf{A}$  is therefore inversely scaled by

$$a_{ij} \mapsto \hat{a}_{ij} = a_{ij} x_i^{\text{ini}} \quad (6)$$

(column-wise scaling), with the purpose of preventing exceedingly large or small  $\hat{x}_i$  to appear numerically.

The typical choice for  $\mathbf{L}$  is a second order finite-difference matrix

$$\mathbf{L}^{(2)} = \begin{pmatrix} -1 & 1 & 0 & \cdots & 0 \\ 1 & -2 & 1 & & \vdots \\ 0 & 1 & -2 & & 0 \\ \vdots & & & \ddots & 1 \\ 0 & \cdots & 0 & 1 & -1 \end{pmatrix} \quad (7)$$

The minimization with respect to the second order derivative describes a continuity constraint that restricts the shape of  $\hat{\mathbf{x}}$  to be cubic spline-like. The simplest  $D$ -dimensional generalization of  $\mathbf{L}^{(2)}$  are the isotropic axial derivatives  $\partial^2/\partial x_k^2, k = 1, \dots, D$ , and the minimization with respect to it behaves similarly to the  $D$ -dimensional cubic tensor splines. We found this type of regularization to be sufficient for the purpose of unfolding multidimensional spectra with Poisson statistics, other choices used e.g. in image restoration are reviewed in [12].

The solution to (4) can be written as a least square problem with the matrix pencil  $(\hat{\mathbf{A}} + \sqrt{\tau}\mathbf{L})$ , and can be solved by a SVD of  $(\mathbf{\Lambda}^{-1}\hat{\mathbf{A}})\mathbf{L}^{-1} = \mathbf{U}\mathbf{\Sigma}\mathbf{V}^T$ , where  $\mathbf{C} = \mathbf{\Lambda}\mathbf{\Lambda}^T$  is the Cholesky decomposition of the measurement covariance, and provided  $\mathbf{L}$  is nonsingular. The software package GURU provides an implementation of this method for diagonal  $\mathbf{C}$  and using  $\mathbf{L}^{(2)}$  (which is strictly speaking singular, but the rectangular nature allows it to be approximately inverted by perturbing  $\mathbf{L}^{(2)} \mapsto \mathbf{L}^{(2)} + \epsilon\mathbf{I}, |\epsilon| \ll 1$ ). However, a  $D$ -dimensional continuity constraint for  $N$  measurements consists of at least  $DN$  axial derivatives and therefore  $\mathbf{L}$  becomes a  $DN \times N$  matrix, it is therefore generally not possible to invert  $\mathbf{L}$  and solve the multidimensional unfolding in the fashion of GURU.

The least square problem with a matrix pencil  $(\mathbf{\Lambda}^{-1}\hat{\mathbf{A}} + \sqrt{\tau}\mathbf{L})$  can also be solved by the generalized SVD (GSVD) [13] of a matrix pair GSVD( $\mathbf{\Lambda}^{-1}\hat{\mathbf{A}}, \mathbf{L}$ ), which simultaneously decomposes both matrices into

$$\begin{aligned} \mathbf{\Lambda}^{-1}\hat{\mathbf{A}} &= \mathbf{U} \begin{pmatrix} 0 & \mathbf{\Sigma}_1 \end{pmatrix} \mathbf{X}^{-1} \\ \mathbf{L} &= \mathbf{V} \begin{pmatrix} 0 & \mathbf{\Sigma}_2 \end{pmatrix} \mathbf{X}^{-1}. \end{aligned} \quad (8)$$

GSVD( $\mathbf{\Lambda}^{-1}\hat{\mathbf{A}}, \mathbf{L}$ ) is therefore closely related to SVD( $(\mathbf{\Lambda}^{-1}\hat{\mathbf{A}})\mathbf{L}^{-1}$ ), which can be immediately seen by comparing the GSVD of the quotient matrix  $(\mathbf{\Lambda}^{-1}\hat{\mathbf{A}})\mathbf{L}^{-1} = \mathbf{U}(\mathbf{\Sigma}_1\mathbf{\Sigma}_2^{-1})\mathbf{V}^T$  ( $\mathbf{L}^\dagger$  being the  $(\mathbf{\Lambda}^{-1}\hat{\mathbf{A}})$ -weighted pseudoinverse of  $\mathbf{L}$  [14]) to the ordinary SVD form  $(\mathbf{\Lambda}^{-1}\hat{\mathbf{A}})\mathbf{L}^{-1} = \mathbf{U}\mathbf{\Sigma}\mathbf{V}^T$ .

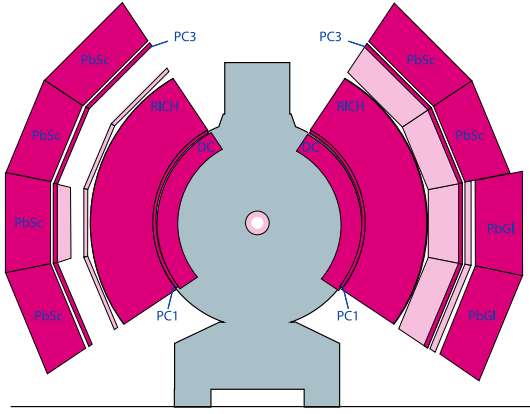


**Figure 1.** The PHENIX central arm detectors for RHIC Run-5 (year 2004/2005), viewed along the beam axis from the south towards north. Dark regions indicate detectors used for the jet reconstruction: The drift chamber (DC), the pad chamber layers 1 and 3 (PC1/PC3), the ring-imaging Čerenkov detector (RICH), and the Pb scintillator (PbSc) and Pb glass (PbGl) electromagnetic calorimeters.

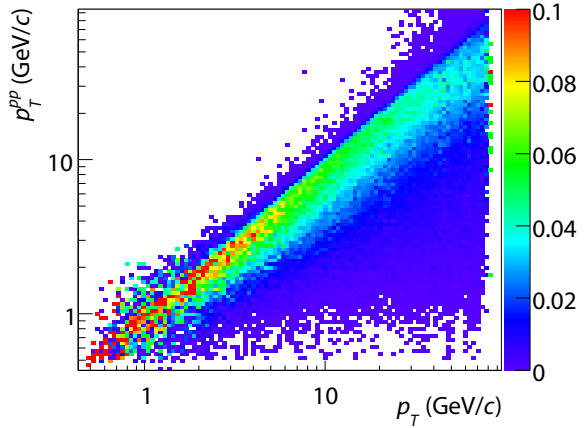


**Figure 2.** The PHENIX jet  $P(p_T^{pp}|p_T)$  transfer matrix for  $\sqrt{s} = 200$  GeV and  $\sigma = 0.3$  Gaussian filter, derived from the GEANT simulation of  $\approx 1.6 \times 10^7$  PYTHIA events. The  $p_T^{pp} < p_T$  region is dominated by  $n$ ,  $K_L^0$  energy loss.

With the generalized singular value pairs  $\mathbf{\Sigma}_1 = \text{diag}(\alpha_i)$ ,  $\mathbf{\Sigma}_2 = \text{diag}(\beta_i)$ , the SVD singular values of  $(\mathbf{\Lambda}^{-1}\hat{\mathbf{A}})\mathbf{L}^\dagger$  are  $\gamma_i = \alpha_i/\beta_i$ . The solution then can be written as the Tikhonov filter for the singular values

$$\mathbf{\Sigma}'^{-1} = \text{diag}\left(\frac{\gamma_i^2}{\gamma_i^2 + \tau}\alpha_i^{-1}\right), \quad (9)$$

and the mean and covariance matrix of the unfolding solution is

$$\begin{aligned} \hat{\mathbf{x}} &= \mathbf{X}\mathbf{\Sigma}'^{-1}\mathbf{U}^T(\mathbf{\Lambda}^{-1}\mathbf{b}) \\ \text{Cov } \hat{\mathbf{x}} &= \mathbf{X}\mathbf{\Sigma}'^{-1}(\mathbf{\Sigma}'^{-1})^T\mathbf{X}^T. \end{aligned} \quad (10)$$

We implemented this multidimensional generalization to GURU's regularized linear least square unfolding based on LAPACK's DGGSD [15], which implements the dense GSVD algorithm by Bai, Demmel & Zha [16, 17].

#### 4. Experimental setup

Figure 1 shows the Run-5 PHENIX “central arm” configuration for RHIC Run-5 (year 2004/2005). PHENIX has two mid-rapidity spectrometers with an aperture of  $|\eta| < 0.35$  and  $\Delta\phi = \pi/2$  each. The components used for jet reconstruction are the drift chamber (DC), the pixel pad chamber layers 1 and 3 (PC1/PC3), the ring-imaging Čerenkov detector (RICH), and the electromagnetic calorimeters (EMCal). For the data presented in this paper, DC/PC1/PC3 provide momentum measurement for charged particles, and the EMCal the energy for photons.

Pattern recognition and momentum reconstruction in the tracking system formed by DC and PC1/3 is performed using the combinatorial Hough transform, with the momentum scale determined by the time-of-flight measurement of identified  $\pi^\pm$ ,  $K^\pm$ , and  $p/\bar{p}$ . The momentum

resolution of the tracking system is determined as  $\delta p/p = 0.7\% \oplus 1.0\% p/(\text{GeV}/c)$ . Two calorimeter technologies were used, six of the total eight sectors are covered by Pb-scintillator (PbSc) calorimeters with resolution of  $\sigma_E/E = 8.1\%/\sqrt{E} \oplus 2.1\%$  and a granularity of  $\Delta\eta \times \Delta\phi \approx 0.01 \times 0.01$ , and two sectors by Pb-glass (PbGl) calorimeters with  $\sigma_E/E = 5.9\%/\sqrt{E} \oplus 0.8\%$  and  $\Delta\eta \times \Delta\phi \approx 0.008 \times 0.008$ . The intrinsic timing resolution for 1 GeV  $\pi^\pm$  are about 200–300 ps for both technologies.

Since PHENIX currently lacks an in-field tracking capability, conversion electrons in the DC can produce a displaced track that has the appearance a high  $p_T$  track originating from the event vertex. We use the information from the RICH and  $dE/dx$  measurement to identify and remove these tracks. To provide additional suppression at the cross section level of jets with  $p_T > 20$  GeV, we use the fact that conversion electrons are geometrically unlikely to coincide with the direction of the jet production, and require the reconstructed jet to have a minimum multiplicity of 3 particles measured within a radial angle of  $60^\circ$ , and the charged fraction of the jet  $p_T$  to be below 0.9 to remove single track events, or when the jet is dominated by a large  $p_T$  track.

The absolute energy scale of the calorimeter clusters are determined using both the reconstructed  $\pi^0$  masses from the observed  $\pi^0 \rightarrow \gamma\gamma$  decays, and checked using the  $E/p$  from energies from cluster matching RICH identified  $e^\pm$  tracks. Shower shape cuts are used to remove clusters. The residual uncertainty in the energy scale is  $\pm 3\%$  (syst.). Since the measurement extends to very low cross sections, processes such as upward beam interaction can deposit energy in the EMCAL that randomly coincides with an event. This is suppressed by measuring the time-of-flight of the clusters and rejecting those that are out of synchronization with the collision.

The PHENIX minimum bias (MB) trigger is defined by the coincident firing of the two beam-beam counters (BBC) located at  $3.0 < \eta < 3.9$ . The Van de Meer/vernier scan method is used to measure the BBC cross section, with  $\sigma_{\text{BBC}} = 22.9 \pm 2.3$  mb (syst.). The efficiency of BBC MB trigger on an event containing a jet with  $p_T^{\text{rec}} > 2$  GeV/ $c$  is  $\epsilon_{\text{BBC}} = 0.86 \pm 0.05$  (syst.) and constant with respect to  $p_T^{\text{rec}}$  within that uncertainty. We require the collision vertex to be within  $|z| < 25$  cm along the beam axis, derived from the timing difference between the firing of the two BBC.

## 5. Inclusive jet cross section in $p + p$

The data presented in the following sections were obtained from the PHENIX  $p + p$  dataset from the RHIC Run-5 (year 2004/2005). After removal of bad quality runs, a total of  $1.47 \times 10^9$  minimum bias  $p + p$  and  $1.16 \times 10^9$  triggered  $p + p$  events are being used.

The measurement of inclusive jet cross section in Run-5  $p + p$  collisions uses the combined minimum bias and triggered data set, and is based on the regularized unfolding of the jet spectrum  $dN_{\text{jet}}/dp_T^{\text{jet,rec}}$  by the jet energy scale transfer function  $P(p_T^{\text{jet,rec}}|p_T^{\text{jet}})$ , which is evaluated by GEANT simulation using PYTHIA 6.4.20 events. A total of  $1.6 \times 10^7$  events were simulated with 14 different minimum  $Q^2$  settings varying between  $\sqrt{Q^2} > 0.5$  GeV/ $c$  and  $\sqrt{Q^2} > 64$  GeV/ $c$ . The resulting transfer matrix  $P(p_T^{\text{pp}}|p_T)$  is shown in figure 2.

The unfolding is equivalent to the inversion of the 1D Fredholm equation

$$\frac{dN_{\text{jet}}}{dp_T^{\text{jet,rec}}} = \int dp_T^{\text{jet}} P(p_T^{\text{jet,rec}}|p_T^{\text{jet}}) \frac{dN}{dp_T^{\text{jet}}}. \quad (11)$$

Then the invariant cross section can be evaluated as

$$\frac{E d^3 \sigma^{\text{jet}}}{dp^3} = \frac{1}{2\pi p_T} \frac{d^2 \sigma^{\text{jet}}}{dp_T^{\text{jet}} dy} = \frac{\sigma_{\text{BBC}}}{A \epsilon_{\text{BBC}}} \frac{1}{p_T^{\text{jet}}} \frac{1}{N_{\text{evt}}} \frac{dN^{\text{jet}}}{dp_T^{\text{jet}}} \quad (12)$$

where  $dN/dp_T$  is the unfolding result from (11) and

$$A = 2(\Delta\eta - 2d)(\Delta\phi/2 - 2d) \quad (13)$$

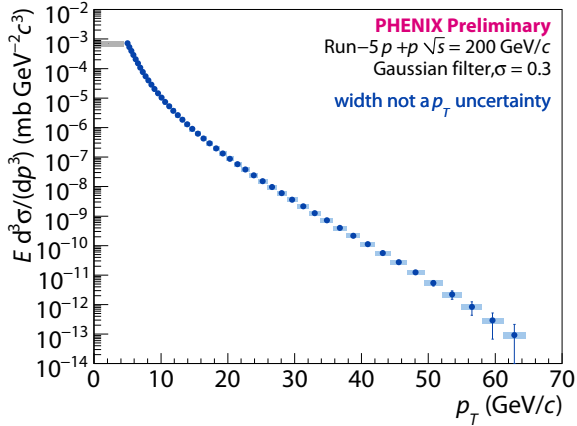


**Figure 3.** PHENIX Run-5  $p + p$  at  $\sqrt{s} = 200$  GeV invariant jet cross section spectrum as a function of  $p_T$ . The shaded box to the left indicates the overall normalization systematic uncertainty, shaded boxes associated with data points indicate point-to-point systematic uncertainties, and error bars indicate statistical uncertainties.

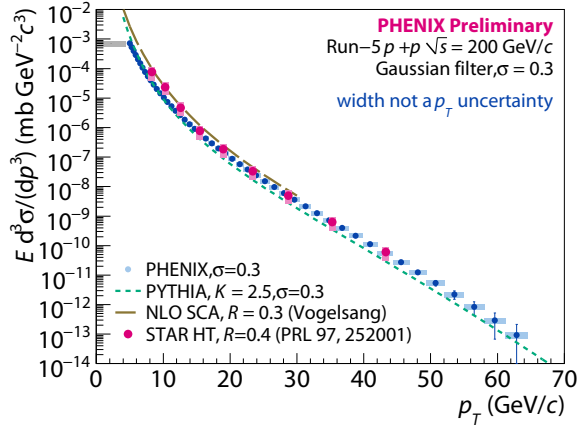


**Figure 4.** PHENIX Run-5  $p + p$  at  $\sqrt{s} = 200$  GeV invariant jet cross section spectrum as a function of  $p_T$ , with comparison to [18], next-to-leading order calculation from [19], and PYTHIA assuming  $K = 2.5$ . The shaded box to the left indicates the overall normalization systematic uncertainty, shaded boxes associated with data points indicate point-to-point systematic uncertainties, and error bars indicate statistical uncertainties.

the fiducially reduced PHENIX central arm acceptance area. This measurement is detailed in [5].

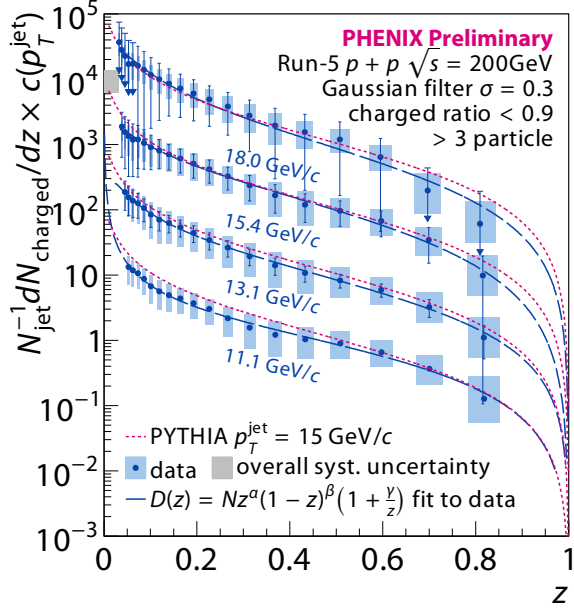
The choice of regularization parameter  $\tau$  can translate into an uncertainty on the low frequency, global shape of a spectrum. We address this by evaluating the systematic uncertainty from varying  $\tau$  over the entire meaningful range between  $\approx 4^D$  degrees of freedom up to the Nyquist frequency,  $D$  being the unfolding dimension.

Figure 3 shows the PHENIX preliminary  $p + p$  jet spectrum measured using the Gaussian filter, plotted in invariant cross sections. The shaded box to the left indicates the overall normalization systematic uncertainty, shaded boxes associated with data points indicate point-to-point systematic uncertainties, and error bars indicate statistical uncertainties. We show the unfolded spectrum out to the  $p_T$  bin where the nominal yield for the number of sampled events reaches the level of 1 jet, namely 60 GeV/c.

Figure 4 shows the same spectrum as in Figure 3, compared against the spectrum from [18], the next-to-leading order (NLO) calculation using the small cone approximation (SCA) [19], and the leading order PYTHIA spectrum assuming  $K = 2.5$ . The comparison to [18] and NLO SCA involve different jet definitions, a residual difference should be expected, even though for  $p_T > 15$  GeV/c it appears to be small between filter and cone jets for the Gaussian size  $\sigma = 0.3$  used in this analysis. Our spectrum is close to [18] within its  $p_T$  reach. The spectrum also follows approximately the shape of the NLO SCA calculation, and the leading order PYTHIA spectrum, if  $K = 2.5$  is assumed. However, a more appropriate comparison would involve Gaussian filter based NLO calculations, which we plan to perform in the future.

## 6. Fragmentation functions in $p + p$

We use the Run-5  $p + p$  minimum bias data set for the measurement of the fragmentation function. For reconstructed jets, we measure the longitudinal contribution of the fragment



**Figure 5.** PHENIX Run-5  $p+p$  at  $\sqrt{s} = 200$  GeV charged (with electron rejection) jet fragmentation function with respect to  $z = w_{\text{filter}} p_{\parallel} / p^{\text{jet}}$  and vertically scaled by  $c(p_T^{\text{jet}}) = 10^k, k = 0, \dots, 3$ . The shaded box to the left indicates the overall normalization systematic uncertainty, shaded boxes associated with data points indicate point-to-point systematic uncertainties, and error bars indicate statistical uncertainties. Biases from the jet level cuts are fully quantified in the systematic uncertainties. The blue curve indicates the  $D(z) = Nz^{\alpha}(1-z)^{\beta}(1+\frac{z}{z_0})$  fit to data, while the red curve shows the same fit from PYTHIA at  $p_T^{\text{jet}} = 15$  GeV/ $c$ .

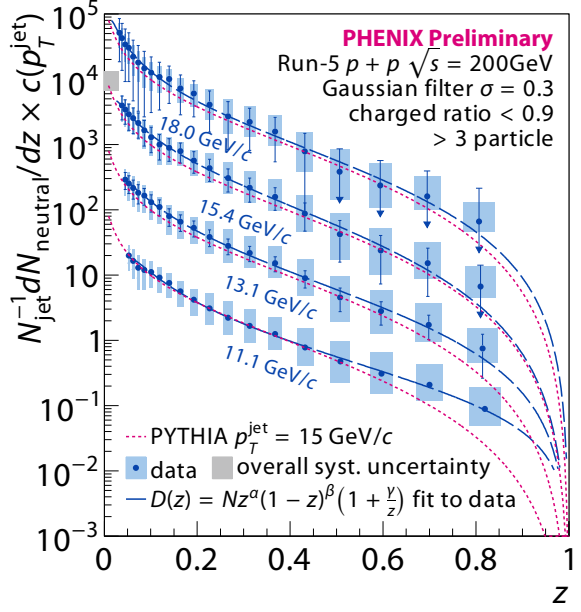


**Figure 6.** PHENIX Run-5  $p+p$  at  $\sqrt{s} = 200$  GeV (electromagnetic) neutral jet fragmentation function with respect to  $z = w_{\text{filter}} p_{\parallel} / p^{\text{jet}}$  and vertically scaled by  $c(p_T^{\text{jet}}) = 10^k, k = 0, \dots, 3$ . The shaded box to the left indicates the overall normalization systematic uncertainty, shaded boxes associated with data points indicate point-to-point systematic uncertainties, and error bars indicate statistical uncertainties. Biases from the jet level cuts are fully quantified in the systematic uncertainties. The blue curve indicates the  $D(z) = Nz^{\alpha}(1-z)^{\beta}(1+\frac{z}{z_0})$  fit to data, while the red curve shows the same fit from PYTHIA at  $p_T^{\text{jet}} = 15$  GeV/ $c$ .

momentum to the jet as

$$z = w_{\text{filter}}(\Delta R) \frac{p_{\parallel}}{p^{\text{jet}}} = \exp\left(-\frac{\Delta\eta^2 + \Delta\phi^2}{2\sigma_{\text{filter}}^2}\right) \frac{\mathbf{p} \cdot \mathbf{p}^{\text{jet}}}{(p^{\text{jet}})^2}. \quad (14)$$

This choice preserves the identity  $\sum z = 1$  for a weighted jet definition, compared to traditional algorithms that would assign zero or unitary weights for nonconstituent and constituent fragments. For practical purpose, both  $p_{\parallel}$  and  $p_T^{\text{jet}}$  are binned logarithmically in the  $dN/(dp_{\parallel} dp_T^{\text{jet}})$  distribution, which allows the  $p_{\parallel}/p_T$  division to be performed as bin shifts. For the narrow mid-pseudorapidity acceptance of the PHENIX central arms, the difference in  $z = p_{\parallel}/p^{\text{jet}}$  and  $z = p_{\parallel}/p_T^{\text{jet}}$  division is  $\leq 6\%$  and negligible within our uncertainties.

We use RICH to reject electrons for the measurement of charged fragmentation function, since in PHENIX, they are produced predominantly from  $\gamma$  conversions in the beam pipe and

Dalitz decays, therefore not associated with the charged fragmentation of jets. At the moment, we also do not reconstruct  $\gamma$  pairs from  $\pi^0$  decays, although we envision to provide identified neutral fragmentation function measurements in the future.

Since the PHENIX detector resolution for single particle far exceeds the resolution for jet energy, we assume a diagonal transfer function for particle energies in the transfer function

$$P(p_T^{\text{jet,rec}}, p_{\parallel}^{\text{rec}} | p_T^{\text{jet}}, p_{\parallel}) = P(p_T^{\text{jet,rec}} | p_T^{\text{jet}}, p_{\parallel}) \delta(p_{\parallel}^{\text{rec}} - p_{\parallel}), \quad (15)$$

although the use of a full transfer function is planned for the future. The same GEANT simulation result as for the jet spectrum is used to evaluate the so reduced conditional transfer function  $P(p_T^{\text{jet,rec}} | p_T^{\text{jet}}, p_{\parallel})$ .

The  $(p_T^{\text{jet}}, p_{\parallel})$  distribution is then unfolded by the regularized inversion of the 2D equation

$$\frac{dN}{dp_T^{\text{jet,rec}} dp_{\parallel}^{\text{rec}}} = \iint dp_T^{\text{jet}} dp_{\parallel} P(p_T^{\text{jet,rec}}, p_{\parallel}^{\text{rec}} | p_T^{\text{jet}}, p_{\parallel}) \frac{dN}{dp_T^{\text{jet}} dp_{\parallel}}. \quad (16)$$

Similarly, the jet spectrum is unfolded by inverting (11). The per-jet normalized fragmentation function is then extracted by dividing the unfolded  $(p_T^{\text{jet}}, p_{\parallel})$  distribution by the unfolded jet spectrum:

$$D(z) = \frac{1}{\epsilon(z, p_T^{\text{jet}})} \left( \frac{dN_{\text{jet}}}{dp_T^{\text{jet}}} \right)^{-1} \frac{dN}{dp_T^{\text{jet}} dz} = \frac{1}{\epsilon(z, p_T^{\text{jet}})} \left( \frac{dN_{\text{jet}}}{dp_T^{\text{jet}}} \right)^{-1} p^{\text{jet}} \frac{dN}{dp_T^{\text{jet}} dp_{\parallel}} \Bigg|_{z=p_{\parallel}/p^{\text{jet}}} \quad (17)$$

where  $\epsilon(z, p_T^{\text{jet}})$  is the single particle efficiency evaluated by GEANT simulation. While the efficiency for neutral clusters are constant at  $\epsilon = 0.81 \pm 0.04$  (syst.), the efficiency for charged tracks exhibits a strong  $z$ -dependence both due to the magnetic field causing low  $p_T$  tracks to be bend out of the azimuthal acceptance, and tracking cuts resulting in the rejection of high  $p_T$   $\pi^{\pm}$  misidentified as electrons. For  $p_T^{\text{jet}} = 18 \text{ GeV}/c$ , the efficiency for charged tracks saturates for  $z > 0.3$  to  $\epsilon = 0.58 \pm 0.06$  (syst.).

Figure 5 shows the  $p + p$  at  $\sqrt{s} = 200 \text{ GeV}$  charged (with electron rejection) jet fragmentation function, vertically scaled by  $c(p_T^{\text{jet}}) = 10^k$ ,  $k = 0, \dots, 3$ . The shaded box to the left indicates the overall normalization systematic uncertainty, shaded boxes associated with data points indicate point-to-point systematic uncertainties, and error bars indicate statistical uncertainties. Biases from the jet level cuts are fully quantified in the systematic uncertainties. The blue curve indicates the  $D(z) = Nz^{\alpha}(1-z)^{\beta} (1 + \frac{z}{z_0})$  fit to data, while the red curve shows the same fit from PYTHIA at  $p_T^{\text{jet}} = 15 \text{ GeV}/c$ .

Figure 6 shows the same plot, for the  $p + p$  at  $\sqrt{s} = 200 \text{ GeV}$  (electromagnetic) neutral jet fragmentation function. In both set of fragmentation measurements, the fragmentation function for  $p_T^{\text{jet}} \geq 15 \text{ GeV}/c$  agree well within our current uncertainty with PYTHIA. We could reach a maximum  $z \approx 0.81$  with our measurement.

## 7. Summary

We presented the first measurement of jet fragmentation function in  $p + p$  collisions performed at RHIC. It demonstrates for the ability of PHENIX to access high- $z$  jet fragmentation property for both charged particles and photons. Techniques to unfold multidimensional spectra such as the fragmentation function has been discussed, which significantly facilitated us to make such a measurement.

Restricting the data to the minimum bias set currently constrains our statistics and ability to lower the unfolding systematic uncertainty. Our current development of the trigger efficiency correction for fragmentation function measurement would allow us to address this problem in the future.



## References

- [1] Adler S S *et al.* (PHENIX) 2006 *Phys. Rev. D* **74** 072002
- [2] Adare A *et al.* (PHENIX) 2009 *Phys. Rev. C* **80** 024908
- [3] Lai Y s and Cole B A 2008 (*Preprint arXiv:0806.1499*)
- [4] Lai Y s (PHENIX) 2009 *Nucl. Phys. A* **830** 251c–254c
- [5] Lai Y s (PHENIX) 2009 (*Preprint arXiv:0911.3399*)
- [6] Cheng Y z 1995 *IEEE Trans. Pattern Anal. Mach. Intell.* **17** 790–799
- [7] Fashing M and Tomasi C 2005 *IEEE Trans. Pattern Anal. Mach. Intell.* **27** 471–474
- [8] Salam G P and Soyez G 2007 *J. High Energy Phys.* **2007** JHEP05(2007)086
- [9] Phillips D L 1962 *J. ACM* **9** 84–97
- [10] Tychonoff A N 1963 *Dokl. Akad. Nauk SSSR* **151** 501–504
- [11] Höcker A and Kartvelishvili V 1996 *Nucl. Instrum. Methods A* **372** 469–481
- [12] Karayiannis N B and Venetsanopoulos A N 1990 *IEEE Trans. Acoust. Speech Signal Processing* **38** 1155–1179
- [13] Van Loan C F 1976 *SIAM J. Numer. Anal.* **13** 76–83
- [14] Eldén L 1982 *BIT Numer. Math.* **22** 487–502
- [15] Anderson E *et al.* 1999 *LAPACK Users' Guide* 3rd ed (Philadelphia, PA: SIAM)
- [16] Bai Z j and Zha H y 1993 *SIAM J. Sci. Comput.* **14** 1007–1012
- [17] Bai Z j and Demmel J W 1993 *SIAM J. Sci. Comput.* **14** 1464–1486
- [18] Abelev B I *et al.* 2006 *Phys. Rev. Lett.* **97** 252001
- [19] Jäger B, Stratmann M and Vogelsang W 2004 *Phys. Rev. D* **70** 034010